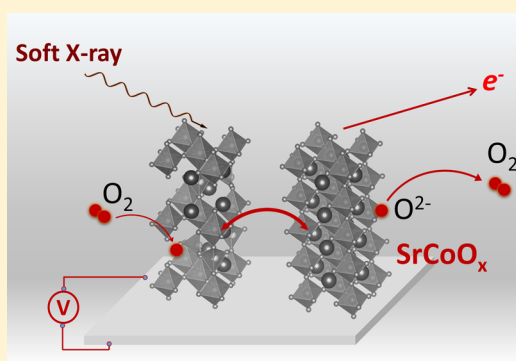


Electronic Structure Evolution of SrCoO_x during Electrochemically Driven Phase Transition Probed by *in Situ* X-ray SpectroscopyQiyang Lu,^{†,‡} Yan Chen,^{†,§,#} Hendrik Bluhm,^{||} and Bilge Yildiz^{*,†,‡,§}[†]Laboratory for Electrochemical Interfaces, [‡]Department of Materials Science and Engineering, and [§]Department of Nuclear Science and Engineering, Massachusetts Institute of Technology, Cambridge, Massachusetts 02139, United States^{||}Chemical Sciences Division, Lawrence Berkeley National Laboratory, 1 Cyclotron Road, MS6R2100, Berkeley, California 94720, United States

S Supporting Information

ABSTRACT: Topotactic phase transition in SrCoO_x ($x = 2.5\text{--}3$, denoted as SCO) has become a focal point for the study of this unique functional oxide system, sparked by the large alteration in the physical and chemical properties from brownmillerite (BM) to perovskite (P) phases. Recently, we showed that applying electrochemical bias could be a convenient way to control the oxygen stoichiometry in SCO and trigger its topotactic phase transition. In this paper, we utilized *in situ* ambient pressure X-ray spectroscopic tools to reveal the electronic structure and oxygen nonstoichiometry evolution during the BM \rightarrow P phase transition of SCO. During the BM \rightarrow P transition via intercalation of oxygen anions into the structure, we found a lowering of the Fermi level due to creation of Co 3d–O 2p hybridized unoccupied states. X-ray absorption spectra showed that the formed unoccupied states have largely O 2p characteristics. Finally, we utilized the time-dependent relaxation of the X-ray absorption intensity as a new approach to study the phase transformation kinetics and rate-limiting mechanisms. The results deepen the understanding of the electronic structure of SCO as a function of its oxygen stoichiometry and phase and may guide the design of SCO properties for electrocatalyst and memristor functionality.



■ INTRODUCTION

Topotactic phase transition of functional oxides induced by changes in oxygen nonstoichiometry can largely alter multiple important physical and chemical properties, including electrical conductivity,¹ magnetic state,^{2,3} and electrocatalytic activity.^{4–6} More importantly, the reversibility of topotactic phase transition enables the reversible controlling and fast switching of highly distinct properties, thus making it appealing for applications such as electrocatalysis⁷ and resistive switching.⁸ In the search of functional oxides with topotactic phase transition behavior, SrCoO_x ($x = 2.5\text{--}3$, denoted as SCO) attracted wide interests due to its unique phase transition between brownmillerite (BM) phase $\text{SrCoO}_{2.5}$ and perovskite (P) phase $\text{SrCoO}_{3-\delta}$. The phase transition between BM-SCO and P-SCO is particularly interesting due to the distinct physical properties between these two phases.^{2,9,10} While BM-SCO shows semiconducting and antiferromagnetic properties at room temperature, P-SCO is a ferromagnetic metallic oxide.¹ This is partially due to the large differences in the structures of BM-SCO and P-SCO. The BM-SCO takes a layered structure with alternating CoO_4 tetrahedral layers and CoO_6 octahedral layers and, more importantly, the so-called structural oxygen vacancy channels in the tetrahedral layers. This brings a structural anisotropy into BM-SCO, which differs from the isotropic cubic structure of P-SCO. The chemical properties,

especially oxygen transport and oxygen reduction/evolution reactivity, are left largely unexplored but are expected to be also highly different between BM-SCO and P-SCO, considering the structurally distinct oxygen sublattices. Therefore, this phase change in SCO, driven by a large change in oxygen nonstoichiometry, is very appealing to multiple applications. It has been reported by Tambunan et al. that SCO can serve as the active material in memristive devices.⁸ Upon application of electrical bias, the local formation of P-SCO conductive filament was believed to be the underlying mechanism for transition from the high resistance state to the low resistance state. Ezbiri et al.⁷ computationally predicted and experimentally confirmed the potential of SCO as an excellent candidate material for thermochemical oxygen separation. Moreover, Jeon et al.¹ showed that the reversible phase transition of epitaxial SCO thin films could be easily triggered at relatively low temperature. It also has been found that SCO thin films could serve as a catalyst for the carbon monoxide oxidation reaction.¹ This wide spectrum of examples all leverage the reversible phase transition of SCO and the consequently large change in oxygen nonstoichiometry and physical properties.

Received: July 27, 2016

Revised: September 23, 2016

Published: September 30, 2016

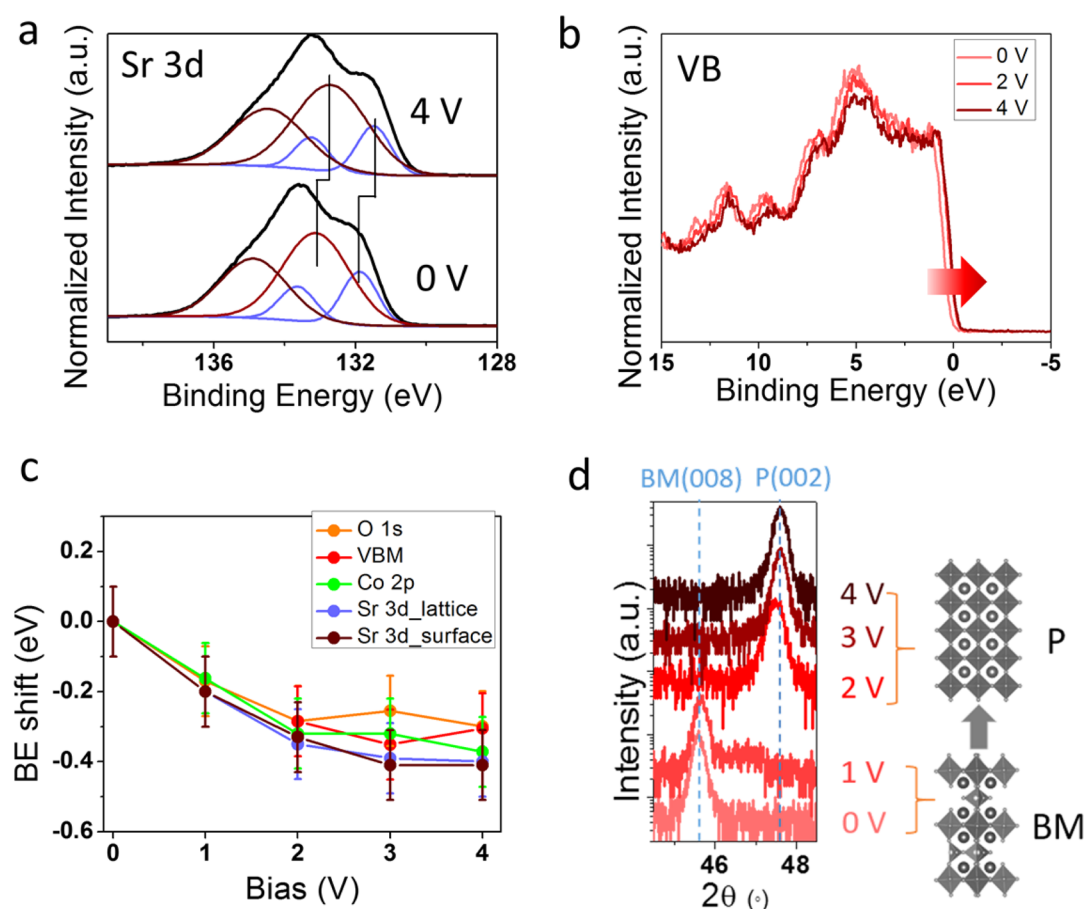


Figure 1. (a, b) X-ray photoemission spectra evolution as a function of applied external bias at 300 °C, 760 mTorr p_{O_2} : (a) Sr 3d; (b) valence band (VB). Sr 3d spectra envelope is fitted with two groups of Sr 3d doublets: one to represent the Sr 3d_lattice shown in light blue and one for Sr 3d_surface shown in dark blue. Detailed Sr 3d, O 1s, and Co 2p XPS peaks are shown in Figure S1. The arrows indicate a shift to lower binding energy (BE) with increasing bias (the rigid shift in the BE has been subtracted according to the biases applied). (c) BE shift as a function of applied bias summarized together for Sr 3d (both lattice and surface species), VB, O 1s, and Co 2p. All the core level and VB spectra BE positions were lowered by roughly the same amount while increasing the bias (within an error bar of ± 0.1 eV). (d) *In situ* X-ray diffraction results recorded under the same conditions as AP-XPS/XAS measurement (300 °C, 760 mTorr p_{O_2}), showing the transition from BM-SCO (indicated by BM(008) diffraction peak) to P-SCO (indicated by P(002) diffraction peak) upon application of a bias higher than 1 V. More details of phase detection by XRD are shown in Figure S2.

Albeit its potential use in multiple applications, practical means to control the topotactic BM \rightarrow P phase transition of SCO has been missing until recently. Early literature showed that extremely high oxygen pressure ($p_{O_2} > 50$ atm) and elevated temperatures (at least 300 °C) are needed to oxidize bulk SCO from BM phase to P phase.² Furthermore, the kinetics for the phase transformation is rather slow, requiring tens of hours for completing the oxidation. More recent work done by Jeon et al. on SCO epitaxial thin films tremendously lowered the transition p_{O_2} (down to ~ 0.67 atm) of BM \rightarrow P phase change and made the kinetics much faster.⁹ Nevertheless, feasible means are needed to reversibly toggle between the two distinct p_{O_2} states (~ 1 and $\sim 10^{-6}$ atm) in order to switch the SCO thin film between the two different phases. Recently, we showed that applying electrochemical potential allows to control the phase of SCO reversibly by tuning the oxygen defect concentration in the oxide.¹¹ The advantage of using electrochemical potential is that the controllable switching between BM and P phases can be achieved without altering the gas pressure or composition in the environment. With *in situ* X-ray diffraction, we demonstrated that the electrochemically

driven BM \rightarrow P transition of SCO can be triggered with an electrochemical potential of merely ~ 22.5 mV in air at 500 °C,¹¹ and the temperature can be lowered down to 300 °C if higher potential is applied. This opened up a new and practical pathway of tuning the properties of functional oxides, while SCO being a very suitable model system.

The oxygen nonstoichiometry in this material has a significant role in determining the electronic and electrocatalytic properties. For instance, the metal–insulator transition induced by the topotactic transition of SCO is the fundamental basis for its promise as a memristive material. For energy storage and conversion applications, oxygen reduction and evolution on SCO involve redox reactions that are strongly influenced by the electronic structure. To date, various important aspects of electronic structure of SCO during phase transition remain unexplored. These include, importantly, the change in Fermi level and the partial density of states (pDOS) of Co and O in valence and conduction bands. One main reason for this is the difficulty of controlling the oxygen nonstoichiometry and phase of SCO while simultaneously investigating the electronic structure. This paper closes the gap on how the electronic structure of SCO evolves during its BM

→ P phase transition by utilizing *in situ* X-ray spectroscopic tools.

In this work, we capture the electronic structure of SCO during its phase transition using ambient pressure X-ray photoelectron spectroscopy (AP-XPS) and X-ray absorption spectroscopy (AP-XAS) under controlled temperature, atmosphere, and electrochemical potential. AP-XPS and resonant photoelectron valence band spectra provided insights into the Fermi level shift and pDOS change in the valence band. AP-XAS, on the other hand, yielded key information on the change in the empty states and the strong hybridization between Co 3d and O 2p orbitals. As a new approach to probing the kinetics and rate-limiting steps of the topotactic phase transition, we used the time-dependent relaxation of the X-ray absorption signatures during the transition from BM to P. The depicted evolution of the electronic structure advances our understanding of the correlation between oxygen defects and the electronic density of states in such a complicated functional oxide system. Moreover, this new knowledge can potentially help to find the ideal functional conditions for SCO in order to enhance its performance in catalytic and memristive applications.

■ RESULTS AND DISCUSSION

Below we show the results obtained on the electronic structure of SrCoO_x using AP-XPS/XAS. First, the shift of Fermi level was probed by recording the binding energy shift of XPS spectra. Second, the change of pDOS in conduction and valence band was assessed by using XAS and resonance photoelectron spectroscopy (RESPES). Finally, we demonstrate the use of the X-ray absorption at O K-edge region as a novel way of monitoring the dynamic process of phase transition.

Fermi Level Shift Revealed by X-ray Core Level Photoelectron Spectra. Figure 1 summarizes the evolution of X-ray core level photoelectron spectra as well as of the valence band (VB) spectra of SCO as a function of applied bias from 0 to 4 V. We note here that the applied electrical bias on the cell is not equal to the electrochemical potential at the SCO electrode because of the voltage loss across YSZ and at the counter electrode. However, with increasing applied electrical bias, the electrochemical potential at the SCO electrode also increases. Therefore, we use the total applied bias to follow the trends in the oxygen defect chemistry and the phase change, which are driven by the electrochemical potential at the SCO electrode. As is evident in Figure 1a,b and Figure S1, all the core level spectra (Sr 3d, O 1s, and Co 2p) and valence band (VB) spectra showed a shift toward lower BE with increasing bias. It is important here to recall that the external electrical bias was applied on the top electrode while the bottom electrode was grounded to the same level as the photoelectron spectrometer. Therefore, the raw data showed a rigid shift in binding energy (BE) that is the same as the applied bias, and the BE axis in Figure 1 was corrected by subtracting the applied bias (1–4 V). After this correction, any shift in BE is attributable to the change in SCO induced by applied bias. In Figure 1c, the BE shifts of each core level or VB spectra are plotted as a function of bias. It can be clearly seen that the shifts for each peak are the same at each bias condition and converge to $\sim 0.3\text{--}0.4$ eV after 2 V. We performed *in situ* X-ray diffraction (XRD) under the same conditions as *in situ* AP-XPS, in order to provide structural information for correctly associating the changes in the electronic structure with phase

and atomic structure. *In situ* XRD showed that SCO remained as the BM phase under 0–1 V, while higher bias (≥ 2 V) induced transition to the P phase (Figure 1d and Figure S2). Therefore, we conclude that the BE shift of $\sim 0.3\text{--}0.4$ eV in Figure 1c corresponds to the BM → P phase transition, and the BE shift does not further change after the P-SCO was stabilized at biases higher than 2 V.

In XPS measurements, the BE in most cases is referenced to the Fermi level of the photoelectron spectrometer. An observed shift in BE can arise from either the change in the core level position (that is, change in the chemical binding environment of a certain element), the Fermi level position, or other effects such as band bending or in-plane voltage loss. If the apparent BE shift affects all core and valence levels in the same way (as shown in Figure 1c), then it should be due to a change in the Fermi level or the potential of the sample or due to band bending and not due to chemical shifts. This is because chemical shifts are in general different for different core levels, which we did not observe in our data. In our case, we argue that band bending is not likely, either. The Sr 3d spectra were fitted with two groups of Sr 3d_{5/2} and 3d_{3/2} peaks (Figure 1b), which can be attributed to two chemical environments of Sr, i.e., the surface species (high binding energy) and the lattice species (low binding energy).^{12,13} The origin of surface species is most likely due to the segregated Sr cations forming secondary phases widely observed on perovskite oxides, such as on $\text{La}_{1-x}\text{Sr}_x\text{CoO}_3$.^{12,13} We observed that the BEs of both the Sr_{surface} and the Sr_{lattice} species were shifted by about the same energy as a function of applied bias, for example, both shifted by 0.4 eV from 0 to 4 V as shown in Figure 1a. This equal shift means that band bending in the near-surface region is not present or is negligible. Despite the possible chemical heterogeneity at the surface laterally, the Sr_{surface} signature comes mostly from the top surface, and Sr_{lattice} has contribution also from the bulk-like subsurface perovskite lattice. In this case, if the band bending were present, effectively the BE shifts of the Sr_{surface} and Sr_{lattice} peaks should have been different, which is opposite to what we observed. Furthermore, the inelastic mean free path (IMFP) for Sr 3d spectra is ~ 1.1 nm, while the Debye length for a metallic system as P-SCO should be subnanometer. This means that the band bending region cannot extend deeper than the probing depth of the Sr 3d photoelectrons (which is 3 times of the IMFP). We also ruled out the role of in-plane voltage loss on SCO thin film on the BE shifts. The electrical conductivity of P-SCO is high at 300 °C ($\sim 10^3$ S/cm). This gives an estimation of in-plane voltage loss on the order of magnitude of 1 mV, which is much lower than the BE shifts we measured. Finally, we also considered the possibility that the change of the Madelung potential from the BM-SCO to the P-SCO, due to the change in oxygen anion coordination, can influence the BE position. However, the BE shifts even before the phase transition (i.e., at an electrical bias of 1 V, Figure 1c), and this shift taking place within the same (BM) phase cannot be explained by the change of Madelung potential. Moreover, if the effect of the change of Madelung potential were significant, then the BE shifts for the two cations (Sr, Co) with different sites and also for the anions (O) are supposed to be different. This is opposite to what we observed (Figure 1c). Based on these two reasons, the possible effect of the Madelung potential change is not significant in interpreting the BE shifts.

After having ruled out the possibility of chemical shifts, band bending, in-plane voltage loss, and an effect of the Madelung

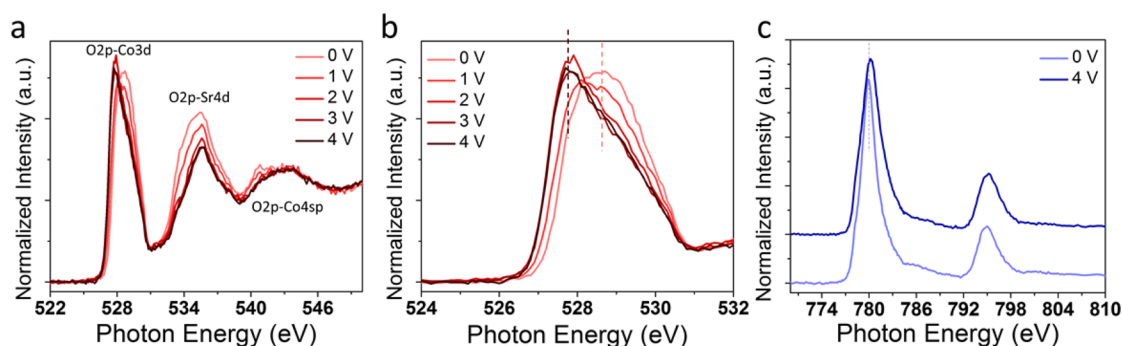


Figure 2. O K-edge and Co L_{2,3}-edge X-ray absorption spectra as a function of applied electrical bias. (a) O K-edge spectra measured under different bias conditions at 300 °C, 760 mTorr p_{O_2} . The three peaks observed correspond to O 2p states hybridized with Co 3d, Sr 4d, and Co 4sp states. (b) Pre-edge peak in O K-edge XAS spectra, showing the evolution of the peak with O 2p–Co 3d characteristics. (c) Co L_{2,3}-edge X-ray absorption spectra without bias applied and with 4 V bias applied. The difference between the peak positions of Co L₃-edge peaks in the two spectra was ~ 0.3 eV. The complete Co L_{2,3}-edge XAS spectra as a function of bias from 0 to 4 V are shown in Figure S5.

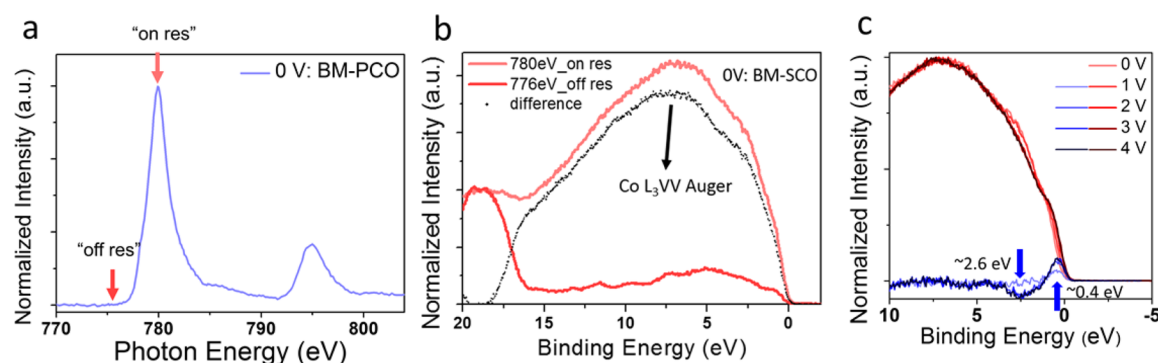


Figure 3. Resonant photoelectron spectroscopy (RESPES) on valence band of SCO. (a) Co L-edge XAS under no bias applied. The arrows indicate the position of the photon energy $h\nu$ used for measuring the VB spectra in (b) and (c); $h\nu = 780$ eV for on-resonance, "on-res", and $h\nu = 776$ eV for off-resonance, "off-res". (b) Comparing the VB spectra excited with $h\nu = 776$ eV ("off res") and $h\nu = 780$ eV ("on res") as well as the difference between two spectra. The core level XPS peak at ~ 19 eV, which contains O 2s and Sr 4p levels, was used to align the intensity of two VB spectra. The enhancement of intensity at "on-res" measurement can be clearly seen, which is partially due to the Co L₃VV Auger peak indicated by the arrow. (c) Evolution of the resonant (on-res) VB spectra as a function of applied bias. The blue lines show the difference spectra with respect to the spectrum with no bias applied.

potential change, we interpret the XPS peak shifts as shifts in the Fermi level, more detailed as following: (1) prior to the BM \rightarrow P phase transition (< 2 V applied biases), there exists a gradual downward shift of Fermi level of SCO; (2) after the phase transition to P-SCO has been completed (≥ 2 V), the Fermi level of P-SCO stays approximately constant, although more oxygen anions are intercalated into the lattice.

The downward shift of Fermi level observed from BM to P phase can be tentatively explained by the charge compensation of intercalated oxygen anions. The intercalated oxygen anions can be regarded as oxygen interstitials for BM-SCO, which should be charge compensated by extra holes. This means more unoccupied states created during the phase transition of SCO, leading to the downward shift of the Fermi level. This is also in line with literature reporting the p-type defect chemistry behavior of $\text{SrCoO}_{3-\delta}$.⁴ We also attempted to obtain an estimation on the change of oxygen nonstoichiometry $\Delta\delta$ during the phase transition of SCO, by using the change of Fermi level and the density of states (DOS) near the Fermi level. The DOS at the Fermi level of $\text{La}_{1-x}\text{Sr}_x\text{CoO}_3$ ($x = 0.2-0.7$) was reported as $\sim 1.1 \text{ eV}^{-1}$ based on the rigid band model (RBM) described by Lankhorst et al.¹⁴ An explicit DOS at Fermi level was not found in the literature for SrCoO_x . If the same RBM was applied to SCO using the DOS of LSC, then

the change in oxygen stoichiometry $\Delta\delta$ at the onset of BM \rightarrow P phase transition should be only $\sim 0.165-0.22$ in our experiment. However, previous experiments suggest that the $\Delta\delta$ at the BM \rightarrow P phase transition should be at least 0.25.^{15,16} We believe that the fundamental source for this discrepancy is that the rigid band model cannot be applied to SCO since the topotactic phase transition has a strong impact on the density of states near the Fermi level, as will be discussed in detail later (Figures 2 and 3). Since the BM-SCO and P-SCO have distinct density of states near the Fermi level, the $\Delta\delta$ calculated using RBM could not yield a correct estimation of the change in nonstoichiometry during the phase transition of SCO.

On the other hand, the Fermi level in P-SCO remains unaltered, even when extra oxide anions are incorporated via applying higher bias. The incorporation of oxygen into the P-SCO is evident from the shrinkage of the lattice parameter (upshift of the 2θ in Figure 1d above 2 V). This is an intriguing behavior. Similarly, a lack of shift in Fermi level accompanying a change in oxygen nonstoichiometry was also recently reported by Nenning et al.¹⁷ on $\text{La}_{0.6}\text{Sr}_{0.4}\text{CoO}_{3-\delta}$ (LSC). It was found that the Fermi level shift of cobaltite (e.g., LSC) as a function of δ in reducing conditions was much smaller compared with other perovskites such as $\text{SrTi}_{0.7}\text{Fe}_{0.3}\text{O}_3$ or $\text{La}_{0.6}\text{Sr}_{0.4}\text{FeO}_3$. Under anodic bias conditions (oxidizing conditions), the Fermi

levels of LSC were roughly constant and did not depend on the increase of oxygen stoichiometry. The origin of this phenomenon is worth further investigation to give a clear answer. Tentatively, one possible explanation of the unchanged Fermi level can be based on the evolution of the electronic structure in P-SCO according to the so-called screened impurity RBM. This model, unlike the RBM mentioned above, suggests that when ionized point defects are created (in our case mainly oxygen vacancies), the entire band will be shifted due to the Coulomb screening of the charged defects.^{18,19} This band shift is in the opposite direction to the shift of Fermi level induced by the concentration change of carrier density due to the charge compensation of the point defects. The screening of the charged defects might be strong enough to cancel out the shift of Fermi level. Therefore, the net result is that in an absolute scale (such as the XPS measurement here) there is no change of the Fermi level, even though more oxygen anions are intercalated which leads to a change of the hole concentration.

Evolution of Unoccupied States and the Oxygen Nonstoichiometry at the Onset of Phase Transition. As mentioned above, the hole concentration was increased during the BM \rightarrow P transition of SCO induced by applied anodic bias. The downward shift of Fermi level indicates the increased population of unoccupied states. In order to clarify the reasons behind the unoccupied state evolution, *in situ* XAS measurements were performed to assess the evolution of the Co oxidation state and the O 2p hole behavior. This also allowed us to deduce an estimated oxygen nonstoichiometry at the onset of phase transition from BM to P phase of SCO. Nominally, the Co valence state changes from Co(III) to Co(IV) when BM-SrCoO_{2.5} is transformed to P-SrCoO₃. However, it is difficult to form Co(IV) with 3d⁵ configuration, and the hybridization between O 2p and Co 3d states can be substantial. Therefore, it is highly likely that the formed unoccupied states may have largely O 2p characteristics, and this is supported by our data below.

Figure 2 shows the O K-edge and Co L-edge XAS evolution under different biases, recorded using partial-electron-yield (PEY) mode. For O K-edge XAS spectra, shown in Figure 2a, three peaks were observed, centered at \sim 528, \sim 535, and \sim 543 eV. These peaks correspond to the empty O 2p states interacting with Co 3d, Sr 4d, and Co 4sp states, respectively. The line shapes of the latter two peaks were not changed under bias. On the contrary, the O 2p–Co 3d peak, i.e., the so-called pre-edge peak, evolved to a completely different line shape up to 2 V accompanying the oxidation of the BM-SCO and phase transformation to P-SCO. After the BM \rightarrow P phase transformation (at biases higher than 2 V), this pre-edge peak did not show any further appreciable change. This is in line with the plateaued Fermi level above 2 V shown in Figure 1c.

The details of the O 2p–Co 3d region of the O K-edge are shown in Figure 2b, and the quantitative assessment of the changes in this region could provide the oxygen nonstoichiometry at the onset of the BM \rightarrow P phase transition of SCO. The pre-edge peak center of BM-SCO is at 527.8 eV. The applied anodic bias shifted this peak toward the lower photon energies and also made the peak highly asymmetric. First, we note that the starting oxygen stoichiometry of our BM-SCO films should be close to 2.5 based on the following comparisons of the O K-edge XAS data in this paper and in reported in the literature. We compared our O K-edge XAS data at 0 V with the data reported by Karvonen et al.²⁰ Our O

K-edge XAS shape is similar to the spectra of SrCoO_{2.5} reported by Karvonen et al., while a higher oxygen stoichiometry causes deviations to the spectra shape, and those deviations are not present in our data. Moreover, there is also a clear similarity between our O K-edge XAS spectra at 0 V with the spectrum of LaCoO₃ reported by Moodenbaugh et al.²¹ In both the LaCoO₃ and SrCoO_{2.5}, Co formal oxidation state is +3. As shown by Moodenbaugh et al., Sr doping into LaCoO₃ caused an increase in Co oxidation state, which also introduced changes in the O K-edge spectra. Our data at 0 V has clear differences from the O K-edge spectra of La_{1-x}Sr_xCoO₃ ($x > 0$). On the basis of these two reasons, we believe the starting oxygen stoichiometry of SCO is close to 2.5.

Next, we recall from Figure 1d that the phase transition from BM to P phase occurs between 1 and 2 V. The shift of the pre-edge peak at 1 and at 2 V was \sim 0.5 and \sim 0.8 eV, respectively, from the 0 V reference state. Previous literature reported that an \sim 1 eV shift for O K-edge XAS spectra corresponds to an increase of the transition metal oxidation state by +1.^{22,23} By applying an interpolation based on this relation of O K-edge XAS to the Co oxidation state, we estimate that $\Delta\delta$ at the onset of phase transition as within the range of 0.25–0.4 and the oxygen stoichiometry falling between SrCoO_{2.75}–SrCoO_{2.9}. The lower limit of this estimated range for $\Delta\delta$ seems reasonable, since it has been reported that an oxygen nonstoichiometry of as high as 0.25 can be stabilized in P-SCO.²⁴ On the other hand, the upper limit of this estimation of $\Delta\delta$ seems to be too high because it would suggest that the SCO would stay in the BM phase until an oxygen nonstoichiometry of \sim 0.1. However, the *in situ* XRD results showed that at 2 V the SCO thin film has been completely transformed to P-SCO, while the BM \rightarrow P phase transition really happened between 1 and 2 V. Therefore, this $\Delta\delta$ of \sim 0.4 is likely to be an overestimation. Finally, we also point out that this estimated range of $\Delta\delta$ has uncertainties because of the fact that the reported correlation between O K-edge peak position and oxidation state of transition metal cation is based on oxide systems without large structural changes. In our case, there is a drastic structural change from BM-SCO to P-SCO, i.e., change of crystal field from mixed tetrahedral and octahedral in BM-SCO to octahedral in P-SCO, which might further complicate the O K-edge spectra.

Unlike the large change in O K-edge shown above, the change in Co L_{2,3}-edge X-ray absorption spectra was relatively subtle. As shown in Figure 2c, the Co L_{2,3}-edge spectra measured under no bias and 4 V bias had roughly similar line shape. However, a noticeable widening of L_{2,3}-edge peak at the higher photon energy side can be clearly seen for the spectra at 4 V bias. Moreover, the peak position was moved toward the higher photon energy by \sim 0.3 eV, which is a relatively small energy shift. This indicates that the applied anodic bias induced an increase in the average Co oxidation state. The largely unaltered edge shape suggests that the Co cations still remained 3d⁶L̄ electronic configuration (L̄ denotes a ligand hole), even after the BM \rightarrow P phase transition. This finding is similar to the reported data on LaFeO₃ and SrFeO₃ by Abbate et al., showing that Fe cation remains 3d⁵L̄ in both LaFeO₃ and SrFeO₃.²⁵ Similar to O K-edge data, there exists a more noticeable change between 1 and 2 V while the Co L_{2,3}-edge spectra under 2–4 V did not show appreciable difference (Figure S5). The branching ratio of Co L-edge XAS (the ratio of intensity between L₃- and L₂-edge) was found as \sim 0.76, and this ratio slightly decreased with increasing electrical bias. Matching the values of the

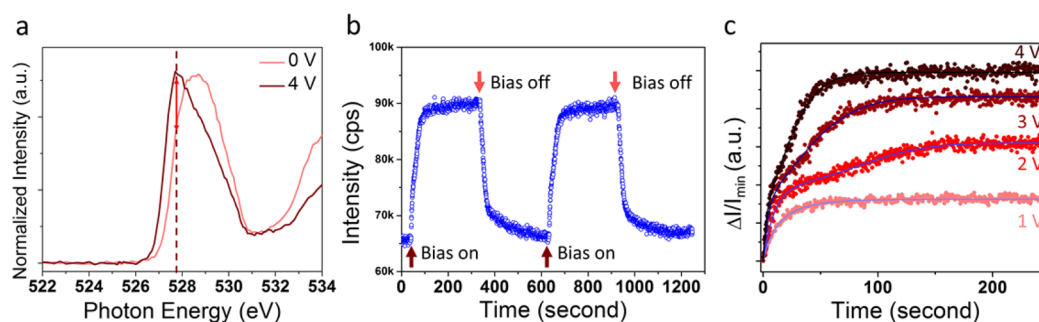


Figure 4. Probing the kinetics of SCO phase transition. Data were collected at $T = 300$ °C and $p_{\text{O}_2} = 760$ mTorr. (a) O K-edge XAS spectra with no bias and with 4 V bias applied. The dashed line indicates the position of the selected photon energy ($h\nu = 527.9$ eV) for the measurement. The large difference in X-ray absorption coefficient for BM and P-SCO is the premise for the dynamic measurement. (b) An example showing the dynamic measurement of the intensity at $h\nu = 527.9$ eV. When the bias was turned on (off), the intensity increased (decreased) following the phase transition process. (c) Evolution of the dynamic measurement, depicted as “intensity difference vs time” curves as a function of bias. The dots are the normalized data while the solid lines are fitting curves using eqs 1 and 2.

branching ratio with the reported values in the literature,²² it is clear that the Co cations are in high-spin (HS) state throughout the experiment. This is not surprising considering the *in situ* XAS data were collected at high temperature ($T = 573$ K).

The drastic change in O K-edge and the relatively unchanged Co L-edge observed here is consistent with the previous *ex situ* XAS results on BM and P-SCO reported by Karvonen et al.²⁰ Furthermore, the recent findings by Mueller et al.²⁶ on multiple perovskite oxides showed that oxygen anions are the more active redox centers rather than transition metal cations, which means extra electron holes can be localized as so-called ligand hole in O 2p orbitals. Our findings reported here provide a new and detailed description of the unoccupied states created by oxygen anion intercalation. These results may also help to identify the ideal functional conditions for SCO in various important applications. For instance, in the research for electrocatalysts, the charge transfer process between gas-phase oxygen molecules and oxide surface is important in determining the kinetics of oxygen reduction/evolution reactions. Oxygen reduction reaction (ORR) is an important electrochemical reaction in solid oxide fuel cells (SOFCs), and it involves electron transfer from oxide electrode to O_2 molecules. To facilitate this reaction, more unoccupied states are needed in the oxide electrocatalyst. We showed the strong O 2p characteristics of the unoccupied states in P-SCO. To increase the rate of ORR, the charge transfer from the ligand holes located on O 2p states to the adsorbed oxygen should be easy. This indicates that the energy level of ligand holes is important in affecting the rate of oxygen reduction or oxygen incorporation into SrCoO_x . More efforts should be directed to the proper design of O 2p ligand level to align with the highest unoccupied molecular orbital (HUMO) of gas phase oxygen. This new strategy, which has also been hinted by several other works in perovskite^{26,27} and Ruddlesden–Popper phase²⁸ oxides, is distinct from the traditional designing criteria that only transition metal is important.²⁹

We also performed fluorescence-yield (FY) XAS measurements, which probe much deeper compared with PEY-XAS results shown in Figure 2. Essentially the FY-XAS results indicate the same features as in the PEY-XAS data for the Co L-edge and O K-edge XAS (see Figure S4). This means that the electronic structure evolution that accompanies the topotactic phase transition is not localized at the near-surface region, but rather is taking place through the whole thin film.

Evolution of the Valence Band Structure. In order to probe the change in valence band structure of SCO during the phase transition, we performed *in situ* resonant photoelectron spectroscopy (RESPES) on VB. This is a useful approach for probing the partial density of states (pDOS) in VB from a certain element. We are specifically interested in Co pDOS in VB, for the reason that it is shown by first-principles computations that the top of VB in SCO has large Co 2p contributions.¹⁰

Figure 3 shows the Co-resonant VB spectra, measured as a function of applied bias. The on-resonance VB spectra were measured by selecting the photon energy as the peak position of Co $\text{L}_{3\text{-edge}}$ XAS peak ($h\nu = 780$ eV) as shown in Figure 3a. The photon energy at the on-resonance position enhances the Co 2p \rightarrow 3d transition and thus increases the intensity of the Co 3d orbital contribution in the valence band. As shown in Figure 3b, the on-resonance VB spectrum had much higher intensity through the whole VB energy range compared with off-resonance VB spectrum. This clearly proves that Co 2p states have a strong contribution to the valence band of SCO. More importantly, we could detect the evolution of the Co pDOS in SCO valence band under anodic bias, as shown in Figure 3c. The differential spectra with respect to the spectrum at 0 V has two features, i.e., an increase in pDOS at ~ 0.4 eV and a decrease at ~ 2.6 eV with respect to the Fermi level. The evolution of these two features as a function of applied bias is likely associated with the change in the crystal field during the phase transition of SCO. BM-SCO has a layered structure with both tetrahedral (T_d) and octahedral (O_h) crystal fields for Co cations. Upon BM \rightarrow P transition, T_d crystal field transforms to O_h coordination. The T_d and O_h crystal fields have different effects on the splitting the Co d orbitals, and the field strength for T_d is much lower than O_h .³⁰ This difference between the T_d and O_h crystal fields is likely to alter the pDOS of Co at the top of VB, thus causing the evolution in RESPES observed as a function of applied bias. Comparing our results with DFT calculations reported by Choi et al.,¹⁰ we can even tentatively link the intensity decrease at ~ 2.6 eV to the diminished T_d -related states and the intensity increase at ~ 0.4 eV to the enhanced O_h -related states, during the BM \rightarrow P phase transition.

Kinetics of SCO Phase Transition Deduced by X-ray Absorption near O K-Edge. The large difference in the line shape of the O K-edge pre-edge peak for BM-SCO and P-SCO, as reported above, allows for extracting the kinetics of this

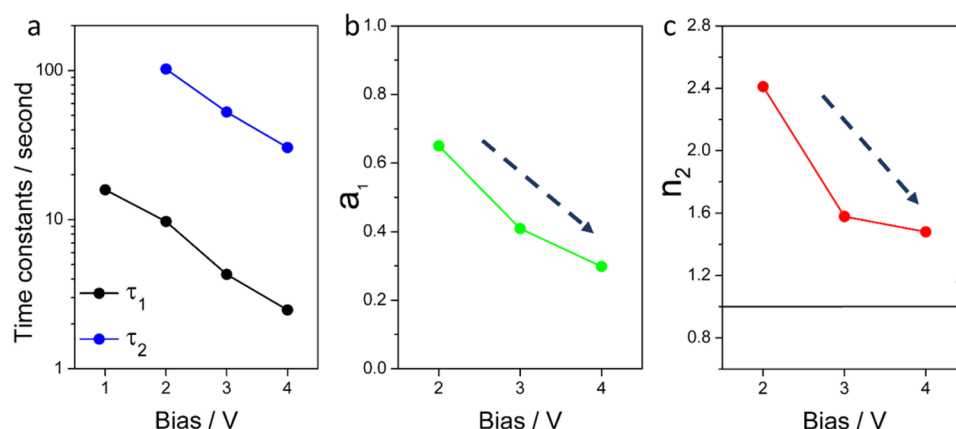


Figure 5. Fitting parameters, including time constants τ_1 and τ_2 (a), relative weight of two exponential terms a_1 (b), and Avrami exponent n_2 (c), obtained from the kinetic data shown in Figure 4c. The solid lines and dashed arrows are guides for the eyes, representing the trend for the change of each fitting parameter.

phase transition. To do so, we monitored the intensity change of the pre-edge peak as a function of time under each applied potential. As shown in Figure 4a, at photon energy of 527.9 eV, the intensities of PEY-XAS are significantly different for BM-SCO and P-SCO. When the anodic bias applied to SCO is high enough to trigger the phase transition from BM to P phase, the intensity will increase. The time-dependent relaxation of this intensity should follow the phase transition process, thus revealing the phase transition kinetics. Vice versa, if the bias is removed, the then XAS intensity at this photon energy drops back to the starting point. One example for this relaxation measurement is shown in Figure 4b, recorded with 4 V bias. The relaxation process can be clearly seen from the two cycles between BM and P phases.

In order to obtain more information about the BM \rightarrow P SCO phase transition kinetics, such as the mechanism and the rate-limiting step, we modeled the normalized intensity–time curves. The model includes two processes, the oxygen incorporation process and the nucleation–growth process, because the phase transition from BM to P phase is driven by the change of nonstoichiometry in SCO. The equation for the modeling the data has the following form:

$$\Delta I(t) = \Delta I_0 \left(1 - a_1 \exp\left(-\frac{t}{\tau_1}\right) - (1 - a_1) \exp\left(-\left(\frac{t}{\tau_2}\right)^{n_2}\right) \right) \quad (1)$$

In eq 1, $\Delta I(t)$ is the time-dependent intensity change during the dynamic measurement and ΔI_0 is a normalization factor. In the time-dependent part, one exponential term and one stretched exponential term are included, with time constants τ_1 and τ_2 , respectively. The weights for the two terms, i.e., a_1 and $1 - a_1$, sum up to give unity. The first term (simple exponential function) is used to describe the oxygen incorporation process, which is driven by the changes in the effective p_{O_2} induced by applied anodic bias. The second term, on the other hand, models the nucleation–growth steps of the BM \rightarrow P phase transition, using the Kolmogorov–Johnson–Mehl–Avrami (KJMA) formalism, with n_2 being the so-called Avrami exponent.³¹ Therefore, the term n_2 contains information on the limiting steps during the phase transitions.

We should note that the data at 1 V electrical bias were treated differently from the relaxation curves under higher biases because 1 V was insufficient to trigger the BM \rightarrow P phase

transition, as seen in the *in situ* XRD data (Figure S3). This is also evident from the different shapes of the relaxation curves. The relaxation curves under biases higher than 1 V all have a change of curvature and highly deviate from simple exponential, while the relaxation curve at 1 V does not show an inflection point. We fit the relaxation curve at 1 V with only one simple exponential, i.e., with only the oxygen incorporation process, in the following form:

$$\Delta I(t) = \Delta I_0 \left(1 - \exp\left(-\frac{t}{\tau_1}\right) \right) \quad (2)$$

We obtained a good fit for data at 1 V by using eq 2, and only one fitting parameter, τ_1 , is used. Therefore, it is only meaningful to limit any trend observed for τ_2 , a_1 , and n_2 to the data points under 2–4 V and compare with data points at 1 V to highlight the difference.

All the relaxation measurement curves in Figure 4c, with bias applied from 2 to 4 V, could be fitted very well using the model in eq 1. The fitting parameters, which are summarized in Figure 5, thus contain important information on the rate-limiting step of the phase transition. First, the two time constants, τ_1 and τ_2 , both decrease monotonically with increasing bias, indicating faster rate for oxygen incorporation and nucleation/growth under higher electrical bias. We can attribute this decrease in τ_1 and τ_2 to the fact that higher p_{O_2} often leads to higher surface exchange rate of oxygen on perovskite oxides.^{32,33} Higher p_{O_2} conditions are effectively obtained by higher anodic biases in our experiment. An alternative explanation is the reaction kinetics follows the Butler–Volmer formalism; i.e., the applied overpotential can drive the reversible reaction to a certain direction exponentially.³⁴ Another finding is that the nucleation/growth process has a much longer time scale than that of the oxygen incorporation process, as τ_2 roughly equals to $10\tau_1$ in each case. The next fitting parameter a_1 , which represents the relative contribution of the oxygen incorporation, also was interestingly shown to decrease with increasing bias. This means that higher bias preferentially facilitates the oxygen incorporation process more compared with the nucleation and growth process. Under higher bias conditions, the nucleation or growth process becomes the main limiting step for electrochemically driven phase transition (with $(1 - a_1) \sim 0.7$ at 4 V). Lastly, we also observed a change in the Avrami exponent n_2 , dropping from ~ 2.4 under 2 V bias to

~ 1.5 under 4 V bias. The change in n_2 indicates a change in the mechanism of nucleation and/or growth, possibly a change in the nucleation rate (constant to decreasing nucleation rate), and/or a change in the growth mode. Future work providing a more microscopic picture should be performed to pinpoint the exact change of mechanism.

Lastly, we note that the same kinetic model should be applicable to tracking the P \rightarrow BM phase transition of SCO when one removes the applied bias, since the reverse phase transition also involves the oxygen exorporation reaction at the surface and the nucleation and growth processes. That is, once the P phase is stabilized with applied bias, one can remove the bias and track the XAS signal as a function of time during the reversal from P to BM and apply the same model on this data to deduce the kinetics. However, the kinetics for oxygen incorporation (BM \rightarrow P) and oxygen exorporation (P \rightarrow BM) reactions can be different, so the resulting limiting step does not have to be the same.

CONCLUSION

In summary, we have revealed several important characteristics of the electronic structure of SCO by performing *in situ* AP-XPS/XAS measurements during the BM \rightarrow P phase transition. AP-XPS captured a downward Fermi level shift characterized by a BE shift of the core level and VB spectra. This shift can be explained by the creation of more empty states in P-SCO upon intercalated oxygen anions. AP-XAS clarified that these created unoccupied states have a strong hybridized Co 3d–O 2p characteristic. We have found the oxygen nonstoichiometry change at the onset of the BM–P phase transition to be within 0.25–0.4, giving a composition of $\text{SrCoO}_{2.75}$ – $\text{SrCoO}_{2.9}$. Compared to the large change in the conduction band structure, only a subtler change in the valence band Co pDOS was observed by RESPEC data. Finally, the distinct conduction band structure between BM-SCO and P-SCO yielded large differences in the X-ray absorption near O K-edge. The time-dependent relaxation of the O K-edge features enabled obtaining information on the rate-limiting steps of the phase transition kinetics. Using this new approach, we found that with increasing bias the nucleation or growth step became more important than the oxygen incorporation process in limiting the kinetics of this electrochemically driven phase transformation.

The combination of AP-XPS/XAS and *in situ* electrochemical biasing, as demonstrated here on SCO, is an illustrative and useful example for studying the electronic structure of functional oxides at a well-controlled oxygen stoichiometry. This methodology can be applied to various technologically important functional oxides to reveal the effect of oxygen nonstoichiometry and phase transitions on their electronic structure. The deepened understanding of the electronic structure can be linked to the performance of the functional oxides in applications such as electrocatalysis or memristors.

EXPERIMENTAL METHODS

SCO Sample Fabrication. Brownmillerite phase $\text{SrCoO}_{2.5}$ (BM-SCO) thin films were fabricated by using pulsed laser deposition (PLD) on 8% yttria-stabilized zirconia (YSZ) substrates with (100) orientation (MTI Corp.). A KrF excimer laser with 248 nm wavelength was used. In order to prevent possible side reaction between SCO and YSZ, an ~ 8 nm 10% gadolinium-doped ceria (GDC) buffer layer was deposited

prior to depositing SCO. The substrate temperature was kept at 750 °C in an oxygen pressure of 20 mTorr. After deposition, we cooled down the samples to room temperature in the same oxygen atmosphere to prevent possible phase change. The thickness of SCO thin film was estimated to be roughly 40 nm. See ref 11 for more details on crystallography, strain state, thickness, and surface morphology of the SCO thin films, which are identical to SCO samples discussed in this current paper. Prior to the SCO deposition, $\text{La}_{0.8}\text{Sr}_{0.2}\text{CoO}_3$ thin film with a thickness of ~ 200 nm was deposited at the backside of YSZ substrates, using the same condition. Therefore, the sample structure can be denoted as SCO/GDC/YSZ/LSC.

***In Situ* Ambient Pressure X-ray Photoelectron/Absorption Spectroscopy (AP-XPS/XAS).** *In situ* XPS/XAS was carried out at Beamline 11.0.2, Advanced Light Source, Lawrence Berkeley National Laboratory. The SCO thin film sample was placed on a customized sample holder with a ceramic heater. A piece of Pt foil was placed in between the heater and SCO sample, in contact with LSC bottom electrode. A thermocouple, along with a small piece of Au foil, was fixed on sample surface with a ceramic piece and clips, which served as top electrode. The Au foil was also used for photon energy calibration by using Au 4f XPS peaks. A Biologic SP-300 potentiostat was used to apply electrochemical bias and perform chronoamperometry measurement. For XPS measurement, Sr 3d and O 1s core level as well as valence band spectra were collected using a photon energy $h\nu$ of 735 eV while the Co 2p core level peak was measured using $h\nu = 985$ eV. The XAS measurements were performed using partial electron yield (PEY) method. The electron kinetic energy windows for Co L-edge and O K-edge XAS were 570 ± 10 and 435 ± 10 eV, respectively. Coresonant VB spectra were collected by choosing $h\nu$ at the maximum intensity in Co L₃-edge XAS spectra.

***In Situ* X-ray Diffraction (XRD).** *In situ* high-temperature XRD measurements were performed on a Bruker D8 Discover X-ray diffractometer equipped with a 4-bounce Ge (022) monochromator. An Anton Parr DHS 900 heating stage was used for sample heating. Electrical leads made from Pt wires and ceramic sheaths were used for the electrical measurements, which are attached to top and bottom electrodes with small amount of silver paint. See ref 11 for more details. The *in situ* XRD measurements were performed at $T = 300$ °C and $p_{\text{O}_2} = 760$ mTorr, which are the same as the conditions for AP-XPS/XAS. Therefore, the results from *in situ* AP-XPS/XAS and XRD can be directly compared to match the changes in crystal structure and electronic structure of SCO.

ASSOCIATED CONTENT

Supporting Information

The Supporting Information is available free of charge on the ACS Publications website at DOI: 10.1021/acs.jpcc.6b07544.

Figures S1–S5 (PDF)

AUTHOR INFORMATION

Corresponding Author

*E-mail byildiz@mit.edu (B.Y.).

Present Address

[#]New Energy Research Institute, School of Environment and Energy, South China University of Technology, Guangzhou Higher Education Mega Center, Guangzhou, Guangdong, China.

Notes

The authors declare no competing financial interest.

ACKNOWLEDGMENTS

The authors acknowledge the funding support from the MIT MRSEC through the MRSEC Program of the National Science Foundation under Award DMR-1419807. The authors also acknowledge the use of the Center for Materials Science and Engineering, an MRSEC facility of NSF at MIT. The Advanced Light Source is supported by the Director, Office of Science, Office of Basic Energy Sciences, of the U.S. Department of Energy under Contract DE-AC02-05CH11231. The authors acknowledge Dr. Christian Lenser and Dr. Mostafa Youssef for insightful discussions.

REFERENCES

- Jeen, H.; Choi, W. S.; Biegalski, M. D.; Folkman, C. M.; Tung, I.-C.; Fong, D. D.; Freeland, J. W.; Shin, D.; Ohta, H.; Chisholm, M. F.; et al. Reversible Redox Reactions in an Epitaxially Stabilized SrCoO_x Oxygen Sponge. *Nat. Mater.* **2013**, *12* (11), 1057–1063.
- Taguchi, H.; Shimada, M.; Koizumi, M. The Effect of Oxygen Vacancy on the Magnetic Properties in the System SrCoO_{3-δ} (0 < δ < 0.5). *J. Solid State Chem.* **1979**, *29* (2), 221–225.
- Hu, S.; Yue, Z.; Lim, J. S.; Callori, S. J.; Bertinshaw, J.; Ikeda-Ohno, A.; Ohkoshi, T.; Yang, C.-H.; Wang, X.; Ulrich, C.; et al. Growth and Properties of Fully Strained SrCoO_x (x ≈ 2.8) Thin Films on DyScO₃. *Adv. Mater. Interfaces* **2015**, *2*, 1500012.
- Chen, D.; Chen, C.; Zhang, Z.; Baiyee, Z. M.; Ciucci, F.; Shao, Z. Compositional Engineering of Perovskite Oxides for Highly Efficient Oxygen Reduction Reactions. *ACS Appl. Mater. Interfaces* **2015**, *7* (16), 8562–8571.
- Sengodan, S.; Choi, S.; Jun, A.; Shin, T. H.; Ju, Y.-W. Y.; Jeong, H. Y.; Shin, J.; Irvine, J. T. S.; Kim, G. Layered Oxygen-Deficient Double Perovskite as an Efficient and Stable Anode for Direct Hydrocarbon Solid Oxide Fuel Cells. *Nat. Mater.* **2014**, *14* (2), 205–209.
- Shin, T. H.; Myung, J.-H.; Verbraeken, M. C.; Kim, G.; Irvine, J. T. S. FD Electrolysis: Oxygen Deficient Layered Double Perovskite as an Active Cathode for CO₂ Electrolysis Using Solid Oxide Conductor. *Faraday Discuss.* **2015**, *182* (0), 227–239.
- Ezbiri, M.; Allen, K. M.; Gálvez, M. E.; Michalsky, R.; Steinfeld, A. Design Principles of Perovskites for Thermochemical Oxygen Separation. *ChemSusChem* **2015**, *8* (11), 1966–1971.
- Tambunan, O. T.; Parwanta, K. J.; Acharya, S. K.; Lee, B. W.; Jung, C. U.; Kim, Y. S.; Park, B. H.; Jeong, H.; Park, J.-Y.; Cho, M. R.; et al. Resistance Switching in Epitaxial SrCoO_x Thin Films. *Appl. Phys. Lett.* **2014**, *105* (6), 063507.
- Jeen, H.; Choi, W. S.; Freeland, J. W.; Ohta, H.; Jung, C. U.; Lee, H. N. Topotactic Phase Transformation of the Brownmillerite SrCoO_{2.5} to the Perovskite SrCoO_{3-δ}. *Adv. Mater.* **2013**, *25* (27), 3651–3656.
- Choi, W. S.; Jeen, H.; Lee, J. H.; Seo, S. S. A.; Cooper, V. R.; Rabe, K. M.; Lee, H. N. Reversal of the Lattice Structure in SrCoO_x Epitaxial Thin Films Studied by Real-Time Optical Spectroscopy and First-Principles Calculations. *Phys. Rev. Lett.* **2013**, *111* (9), 097401.
- Lu, Q.; Yildiz, B. Voltage-Controlled Topotactic Phase Transition in Thin-Film SrCoO_x Monitored by in Situ X-Ray Diffraction. *Nano Lett.* **2016**, *16* (2), 1186–1193.
- Crumlin, E. J.; Mutoro, E.; Liu, Z.; Grass, M. E.; Biegalski, M. D.; Lee, Y.-L.; Morgan, D.; Christen, H. M.; Bluhm, H.; Shao-Horn, Y. Surface Strontium Enrichment on Highly Active Perovskites for Oxygen Electrocatalysis in Solid Oxide Fuel Cells. *Energy Environ. Sci.* **2012**, *5* (3), 6081.
- Tsvetkov, N.; Lu, Q.; Sun, L.; Crumlin, E. J.; Yildiz, B. Improved Chemical and Electrochemical Stability of Perovskite Oxides with Less Reducible Cations at the Surface. *Nat. Mater.* **2016**, *15* (9), 1010.
- Lankhorst, M.; Bouwmeester, H.; Verweij, H. Use of the Rigid Band Formalism to Interpret the Relationship between O Chemical Potential and Electron Concentration in La_{1-x}Sr_xCoO_{3-δ}. *Phys. Rev. Lett.* **1996**, *77* (14), 2989–2992.
- Le Toquin, R.; Paulus, W.; Cousson, A.; Prestipino, C.; Lamberti, C. Time-Resolved in Situ Studies of Oxygen Intercalation into SrCoO_{2.5}, Performed by Neutron Diffraction and X-Ray Absorption Spectroscopy. *J. Am. Chem. Soc.* **2006**, *128* (40), 13161–13174.
- Karvonen, L.; Yamauchi, H.; Karppinen, M. Homologous Series of SrCoO_{(3n-1)/n} Perovskites Obtained Through Br₂ Oxygenation of SrCoO_{2.5}. *Chem. Mater.* **2008**, *20* (22), 7143–7147.
- Nenning, A.; Opitz, A. K.; Rameshan, C.; Rameshan, R.; Blume, R.; Hävecker, M.; Knop-Gericke, A.; Rupprechter, G.; Klötzer, B.; Fleig, J. Ambient Pressure XPS Study of Mixed Conducting Perovskite-Type SOFC Cathode and Anode Materials under Well-Defined Electrochemical Polarization. *J. Phys. Chem. C* **2016**, *120* (3), 1461–1471.
- McKinnon, W. R.; Selwyn, L. S. Ionic and Electronic Contributions to the Li Chemical Potential in Li_xRu₂Mo₆Se₈. *Phys. Rev. B: Condens. Matter Mater. Phys.* **1987**, *35* (13), 7275–7278.
- Friedel, J. Electronic Structure of Primary Solid Solutions in Metals. *Adv. Phys.* **2001**, *50* (6), 539–595.
- Karvonen, L.; Valkeapää, M.; Liu, R. S.; Chen, J. M.; Yamauchi, H.; Karppinen, M. O-K and Co-L XANES Study on Oxygen Intercalation in Parasite SrCoO_{3-δ}. *Chem. Mater.* **2010**, *22* (1), 70–76.
- Moodenbaugh, A.; Nielsen, B.; Sambasivan, S.; Fischer, D.; Friessnegg, T.; Aggarwal, S.; Ramesh, R.; Pfeffer, R. Hole-State Density of La_{1-x}Sr_xCoO_{3-δ} (0 ≤ x ≤ 0.5) across the Insulator/metal Phase Boundary. *Phys. Rev. B: Condens. Matter Mater. Phys.* **2000**, *61* (8), 5666–5671.
- Hu, Z.; Grazioli, C.; Knupfer, M.; Golden, M. S.; Fink, J.; Mahadevan, P.; Kumar, A.; Ray, S.; Sarma, D. D.; Warda, S. A.; et al. Difference in Spin State and Covalence between La_{1-x}Sr_xCoO₃ and La_{2-x}Sr_xLi_{0.5}Co_{0.5}O₄. *J. Alloys Compd.* **2002**, *343* (1–2), 5–13.
- Hu, Z.; Golden, M.; Fink, J.; Kaindl, G.; Warda, S.; Reinen, D.; Mahadevan, P.; Sarma, D. Hole Distribution between the Ni 3d and O 2p Orbitals in Nd_{2-x}Sr_xNiO_{4-δ}. *Phys. Rev. B: Condens. Matter Mater. Phys.* **2000**, *61* (5), 3739–3744.
- Petrie, J. R.; Mitra, C.; Jeen, H.; Choi, W. S.; Meyer, T. L.; Reboredo, F. A.; Freeland, J. W.; Eres, G.; Lee, H. N. Strain Control of Oxygen Vacancies in Epitaxial Strontium Cobaltite Films. *Adv. Funct. Mater.* **2016**, *26*, 1564–1570.
- Abbate, M.; de Groot, F. M. F.; Fuggle, J. C.; Strebel, O.; Lopez, F.; Domke, M.; Kaindl, G.; Sawatzky, G. A.; Takano, M.; Takeda, Y.; et al. Controlled-Valence Properties of La_{1-x}Sr_xFeO₃ and La_{1-x}Sr_xMnO₃ Studied by Soft-X-Ray Absorption Spectroscopy. *Phys. Rev. B: Condens. Matter Mater. Phys.* **1992**, *46* (8), 4511–4519.
- Mueller, D. N.; Machala, M. L.; Bluhm, H.; Chueh, W. C. Redox Activity of Surface Oxygen Anions in Oxygen-Deficient Perovskite Oxides during Electrochemical Reactions. *Nat. Commun.* **2015**, *6*, 6097.
- Orikasa, Y.; Ina, T.; Nakao, T.; Mineshige, A.; Amezawa, K.; Oishi, M.; Arai, H.; Ogumi, Z.; Uchimoto, Y. X-Ray Absorption Spectroscopic Study on La_{0.6}Sr_{0.4}CoO_{3-δ} Cathode Materials Related with Oxygen Vacancy Formation. *J. Phys. Chem. C* **2011**, *115* (33), 16433–16438.
- Nakamura, T.; Oike, R.; Ling, Y.; Tamenori, Y.; Amezawa, K. The Determining Factor for Interstitial Oxygen Formation in Ruddlesden–Popper Type La₂NiO₄-Based Oxides. *Phys. Chem. Chem. Phys.* **2016**, *18*, 1564–1569.
- Bucher, E.; Sitte, W.; Caraman, G. B.; Cherepanov, V. A.; Aksenova, T. V.; Ananyev, M. V. Defect Equilibria and Partial Molar Properties of (La,Sr) (Co,Fe)O_{3-δ}. *Solid State Ionics* **2006**, *177* (35–36), 3109–3115.
- Smith, D. W. Ligand Field Theory & Spectra. In *Encyclopedia of Inorganic Chemistry*; John Wiley & Sons, Ltd.: 2006.
- Avrami, M. Kinetics of Phase Change. I General Theory. *J. Chem. Phys.* **1939**, *7* (12), 1103–1112.

- (32) Lane, J. A.; Benson, S. J.; Waller, D.; Kilner, J. A. Oxygen Transport in $\text{La}_{0.6}\text{Sr}_{0.4}\text{Co}_{0.2}\text{Fe}_{0.8}\text{O}_{3-\delta}$. *Solid State Ionics* **1999**, *121* (1), 201–208.
- (33) Merkle, R.; Maier, J. Oxygen Incorporation into Fe-Doped SrTiO_3 : Mechanistic Interpretation of the Surface Reaction. *Phys. Chem. Chem. Phys.* **2002**, *4* (17), 4140–4148.
- (34) Chueh, W. C.; Haile, S. M. Electrochemistry of Mixed Oxygen Ion and Electron Conducting Electrodes in Solid Electrolyte Cells. *Annu. Rev. Chem. Biomol. Eng.* **2012**, *3*, 313–341.